



ELSEVIER

Journal of Molecular Catalysis A: Chemical 166 (2001) 3–13

JOURNAL OF
MOLECULAR
CATALYSIS
A: CHEMICAL

www.elsevier.com/locate/molcata

Reactivity of methane mono-oxygenase, insights from quantum mechanic studies on synthetic iron model complexes

Peter-Paul Knops-Gerrits^{a,d,*}, Pierre A. Jacobs^b, Atsushi Fukuoka^c,
Masaru Ichikawa^c, Francesco Faglioni^a, William A. Goddard III^a

^a Material and Process Simulation Center, Beckman Institute (139-74), California Institute of Technology, Pasadena, CA 91125, USA

^b Center for Surface Science and Catalysis, Katholieke Universiteit Leuven, Kardinaal Mercierlaan 92, B-3001 Heverlee, Belgium

^c Catalysis Research Center, Hokkaido University, Sapporo 060, Hokkaido, Japan

^d Département de Chimie, Université Catholique de Louvain (UCL), Lavoisier, Place L. Pasteur no. 1, B-1348 Louvain-la-Neuve, Belgium

Abstract

Methane mono-oxygenase (MMO) and deoxyhemerythrin (DHR) are examples of di-iron enzymes that catalyze the dissociative and non-dissociative binding of molecular oxygen. To mimic the MMO active site with a finite cluster, we chose to study the binuclear heptapodate coordinated iron(III)-complexes of *N,N,N',N'*-tetrakis(2-benzimidazolylmethyl)-2-hydroxy-1,3-diamino-propane (HPTB) and *N,N,N',N'*-tetrakis(2-pyridylmethyl)-2-hydroxy-1,3-diamino-propane (HPTP). These have active sites of the form $[\text{Fe}_2(\text{HPTP})(\mu\text{-OH})]^{4+}$ (1) and $[\text{Fe}_2(\text{HPTB})(\mu\text{-OH})]^{4+}$ (2). Quantum mechanics structures are compared with the experimental data obtained from the EXAFS analysis. For the O_2 binding on the reduced active site, the $\mu\text{-}\eta^1\text{:}\eta^1\text{-O}_2$ mode seems the slightly more stable precursor to the $\text{O}=\text{Fe}-\text{O}-\text{Fe}=\text{O}$ bis-ferryl (re)active site. The nature of the ferryl groups are these of a reactive two center three electron bond. © 2001 Elsevier Science B.V. All rights reserved.

Keywords: Methane mono-oxygenase; Quantum mechanics; EXAFS analysis; Reactivity; Structure; Energetics; Orbital description

1. Introduction

Theoretical modeling of the structure and reactivity at enzyme active sites such as methane mono-oxygenase (MMO) is of intrinsic importance in a biological, chemical and industrial context [1–12]. Studies how the dioxygen cleavage [1–4] and methane activation [5–12] on these diiron enzyme core models takes place, has been studied with various methods. Yoshizawa et al. use density functional methods to study dioxygen binding with the extended Hückel

method, an approximate molecular orbital method, which has also been used to study the reactivity with methane [1]. The $\mu\text{-}\eta^1\text{:}\eta^1\text{-O}_2$ binding mode is the most favorable binding mode of dioxygen on complexes on which one bridging ligand is removed [1]. The $\mu\text{-}\eta^1\text{:}\eta^1\text{-O}_2$ mode is most effective for electron transfer to the d-block orbitals. Methane mono-oxygenase and deoxyhemerythrin are examples of diiron enzymes that catalyze the dissociative and non-dissociative binding of molecular oxygen [4–12]. Dissociative binding of oxygen via a peroxo intermediate to a diamond core structure [4] leads to a reactive species active in the oxidation of alkanes [4,5]. Methane mono-oxygenase has a binuclear active site in which two histidines and four glutarates are present. Both iron ions are coordinated by a histidine, an oxygen from a bridging carboxylate and a

* Corresponding author. Tel.: +1-626-395-2731;
fax: +1-626-585-0918.

E-mail addresses: ppkg@wag.caltech.edu, ppkg@chim.ucl.ac.be
(P.-P. Knops-Gerrits).

¹ Tel.: +32-10-472939; fax: +32-10-472330.

μ -oxo bridge [5]. Non-dissociative binding of oxygen via a side-on peroxo intermediate such as in the active site of deoxyhemerythrin does not allow the splitting and allows binding/release of oxygen as a function of the physiological conditions [10]. Such active sites related to oxo- and hydroxo-bridged di- or poly-iron cores in biological systems [8,9] have been recently subject to extensive theoretical modeling [1–3,13–16]. Siegbahn et al. showed that model systems of MMO with only simple aqua and carboxylato ligands having intermediates with plausible energies and structures and a low-energy transition for the C–H abstraction [3]. In these gas-phase calculations, the dielectric constant of the enzyme is low ($\epsilon=4$) compared to this of water ($\epsilon=80$) [3]. For solvation of model compounds in water such effects are not negligible. For the Fe(IV)-complexes 5- or 6-coordination behave as well, for Fe(III)-complexes such as $\text{Fe}(\text{OH})_3(\text{OH}_2)_3$ 5-coordination is favored, whereas for $\text{Fe}(\text{OH}_2)_6$ 6-coordination is observed. For Fe(II)-complexes 4-coordination occurs and extra water molecules are present in a second shell. Regarding methane activation Crabtree [2] reviewed the recent data. According to Siegbahn et al., [3] the most significant structure is the $\text{Fe}^{\text{III}}\text{--O--Fe}^{\text{V}}\text{=O}$ oxo structure. The ground state of this structure is ^1A and the iron spins are 4.00 and 2.94, the spin on the bridging oxygen is 0.76 and on the oxo ligand is as high as 1.13. The oxide cations of iron have a high spin ground state and adjacent low spin excited state and possess the same bonding patterns as the oxygen molecule [17]. Good bonding of the low spin state, leads to a spin cross-over along the reaction coordinate and opens a low-energy TSR (two state reactivity) path for hydroxylation. The mimicking of such enzymes by immobilization of the model complexes [18–23] in the voids of clays or mesoporous

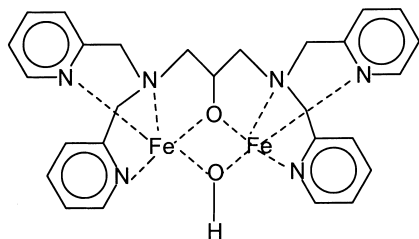


Fig. 1. Structure of $[\text{Fe}_2(\text{HPTP})(\mu\text{-OH})(\text{NO}_3)_2](\text{NO}_3)_2$.

silica–alumina is our interest [24–28]. The characterization of $[\text{Fe}_2(\text{HPTP})(\mu\text{-OH})(\text{NO}_3)_2](\text{ClO}_4)_2$ (1) as seen in Fig. 1 and $[\text{Fe}_2(\text{HPTB})(\mu\text{-OH})(\text{NO}_3)_2](\text{NO}_3)_2$ (2) with EXAFS–XANES, spectroscopic tools and a complimentary theoretical quantum structure analysis is investigated here.

2. Experimental

2.1. Synthesis

2.1.1. $[\text{Fe}_2(\text{HPTB})(\text{OH})(\text{NO}_3)_2](\text{NO}_3)_2$

N,N,N',N' -tetrakis(2-benzimidazolylmethyl)-2-hydroxy-1,3-diaminopropane (HPTB) is prepared [4,18,24]. To an ethanol solution of $\text{Fe}(\text{NO}_3)_3 \cdot 6\text{H}_2\text{O}$ (0.31 g) the HPTB (0.30 g) is added. The precipitated iron complex is collected.

2.1.2. $[\text{Fe}_2(\text{HPTP})(\text{OH})(\text{NO}_3)_2](\text{ClO}_4)_2$

N,N,N',N' -tetrakis(2-pyridylmethyl)-2-hydroxy-1,3-diamino-propane H(HPTP)* as perchlorate is prepared from *p*-chloropicoline and 2-hydroxy-1,3-diaminopropane after [10]. As in the previous synthesis, $\text{Fe}(\text{NO}_3)_3 \cdot 6\text{H}_2\text{O}$ (0.31 g) and H(HPTP)(ClO_4)₂ (0.28 g) are solved in ethanol. The complex is washed with acetonitrile/diethylether and recrystallized in diethylether.

2.2. EXAFS–XANES characterization

EXAFS–XANES X-ray absorption spectra were conducted on beamline BL-7C, under ring conditions of 2.5 GeV, 200–400 mA in the photon factory of the National Laboratory of High Energy Physics (KEK-PF). The radiation was mono-chromatized using a Si(111) double crystal mono-chromator. Data were measured in transmission mode with N_2 -filled ionization chamber of 17 cm and a N_2/Ar (85/15)-filled ionization chamber of 31 cm to $k = 10 \text{ \AA}^{-1}$ for XAS and to $k = 16 \text{ \AA}^{-1}$ for EXAFS. Sample preparation involves pressing BN pellets of a diameter of 6.4 mm with an iron concentration of 10 wt.% for pure samples. Care should be taken in the analysis of highly diluted samples (in HMS or other supported samples) because of the X-ray absorbance of the sample. Energies were calibrated using an internal Fe foil standard, assigning the Fe K-edge to

7111 eV. In the figures the $\chi(k)$ extraction, the Fourier conversion and the McKale spherical wave curve fitting data are shown. EXAFS–XANES file analysis and curve fitting is performed with TECHNOS software, a curve fitting was performed to evaluate the contributions of Fe, C, N and O atoms and their inter-atomic distances.

2.3. Computational analysis

The ab initio calculations used involve full geometry optimization of the clusters with density functional theory (dft) as implemented in Jaguar [15] (Jaguar 3.0, Schrodinger, Inc., Portland, Oregon, 1997) at the B3LYP method level (Becke3 hybridization functionals, Slater/Becke88 non-local exchange and Li, Yang, Parr local and non-local correlation corrections to the local potential energy functionals of Vosko, Wilk and Nusair) using the Los Alamos effective core potential and valence double Zeta for iron (LACVP** basis sets). Calculations are carried out on an Origin2000 (16 MIPS R10000 (IP27) CPU's, 195 MHz w/4 MB secondary cache each, with an IRIX 6.4 S2MP + OCTANE operating system).

The molecular mechanics calculations involve a new molecular mechanics force field, the Universal force field (UFF) of Rappé et al. and co-workers [13,14]. The force field parameters are estimated using general rules based only on the element, its hybridization and its connectivity. The force field functional forms, parameters, and generating formulas for the full periodic table have been published [13]. For charge equilibration used in molecular dynamics simulations, the charges in the complexes are determined [16]. This helps to readjust charges based on geometry and experimental atomic properties.

The initial structures were energy minimized using a suitable set of parameters that are appended to the UFF. These better describe the respective coordination around iron in the model compounds. The quantum mechanical study was performed at the ab initio level starting from a UFF optimized structure. UFF optimization uses a Newton–Raphson minimization scheme with a norm of the gradient convergence criteria of 1×10^{-10} kcal/mol/Å and is verified by the absence of negative Eigen values in the force constant matrix. In order to accommodate the iron in its five coordinate form, as predicted by the EXAFS data, af-

ter UFF optimization, a QM calculation is performed. Atom types for iron and other transition metals in the UFF is given with its symbol, hybridization and valence state. UFF contains 126 atom types, the force constants are generated using Badgers rules as described, the van der Waals parameters are computed based on a Lennard–Jones type potential [13,14].

2.4. Spectroscopic characterization

Diffuse reflectance spectroscopy (DRS) spectra are recorded on a Varian Cary 5 photometer. Mössbauer spectra are recorded on a horizontal constant acceleration drive in transmission geometry with a 150 mCi $^{57}\text{Co}(\text{Rh})$ source. The 14.4 keV Mössbauer transition of the lowest excited level of ^{57}Fe to its ground state ($E_e - E_g = 14.4$ keV, $t_{1/2} = 98$ ns and natural linewidth = 4.7×10^{-9} eV) is fed by the decay of ^{57}Co ($t_{1/2} = 270$ days). MS is a microscopic, nuclear technique, based on the recoilless emission and absorption of γ -rays by a 'source' and an 'absorber'. MS determines the recoilless fraction (or f-fraction) and the hyperfine parameters (isomeric shift δ , quadrupolar splitting Δ and the magnetic splitting) of the MS-nucleus. SQUID spectra are recorded on an MPMS SQUID spectrometer of quantum design. EPR spectra are recorded on a Varian E-line spectrometer, with a liquid He cooling attachment.

3. Results and discussion

3.1. EXAFS spectroscopy

The Fe K-edge EXAFS–XANES analysis gives direct information of the coordination environment of the complexes as salts. The Fe K-edge XAS on $[\text{Fe}_2(\text{HPTP})(\mu\text{-OH})(\text{NO}_3)_2](\text{NO}_3)_2$ and $[\text{Fe}_2(\text{HPTB})(\mu\text{-OH})(\text{NO}_3)](\text{NO}_3)_2$ show pre-edge features indicative of a distorted five coordinated iron with a sixth Fe-ligand, the edge-shifts of 13.1 and 15.5 eV are characteristic for its high spin ferric form. The EXAFS region is informative for a number of parameters including coordination number (CN), inter-atomic distance (R), correction of threshold energy (ΔE), and difference of the Debye–Waller factor from reference compounds ($\Delta\sigma^2$) derived by the analysis of EXAFS spectra. As seen in

Table 1
Fourier transform range Fe K-edge EXAFS analysis

Samples	Shell	R^a (Å)	CN ^b	σ^c	ΔE^{0d} (eV)	Residual ^e
HPTB/Fe	Fe–Fe	3.233	1	0.062	–1.34	7.76
	Fe–O	1.933	1	0.025	–7.33	2.89
	Fe–O	1.919	1	0.128	14.11	
	Fe–N	2.105	2	0.048	14.39	
	Fe–N	2.327	1	0.016	9.92	
HPTB/Fe/HMS ^f	Fe–Fe	3.347	1 ^g	0.049	7.05	11.96
	Fe–N/O	2.25	5	n.d.	n.d.	
HPTP/Fe	Fe–Fe	3.020	1	0.130	–0.99	16.8
	Fe–O	1.929	1	0.055	–9.65	9.47
	Fe–O	1.936	1	0.120	16.92	
	Fe–N	2.185	2	0.073	18.41	
	Fe–N	2.384	1	0.115	10.74	
HPTP/Fe/HMS ^f	Fe–Fe	3.216	1 ^g	0.119	2.10	11.46
	Fe–N/O	2.25	3	n.d.	n.d.	
	Fe–O	1.99	2	n.d.	n.d.	

^a Inter-atomic distance.

^b Coordination number.

^c Debye–Waller factor.

^d Energy (eV).

^e R factor (%).

^f Hexagonal mesoporous silica.

^g Using the TECHNOS software. Sometimes a slightly larger value (up to 1.25) may reflect iron aggregation and silicon/aluminum coordination.

Table 1, the Fe K-edge EXAFS indicates that the $[\text{Fe}_2(\text{HPTP})(\mu\text{-OH})]^{4+}$ gives a coordination number (CN) of 1 for the Fe–Fe bonding and an Fe–Fe distance of 3.020 Å, the $[\text{Fe}_2(\text{HPTB})(\mu\text{-OH})]^{4+}$ gives a CN of 1 for the Fe–Fe bonding and an Fe–Fe distance of 3.233 Å in accordance with the crystallographic data [18–20]. For complexes with bulkier HPTB ligands $\mu\text{-OH}$ species are seen in the Mössbauer spectra due to longer Fe–Fe distances, with less bulky HPTP ligands, two species with longer and shorter Fe–Fe distances are seen, in Table 2, closer to $\mu\text{-OH}$ and $\mu\text{-O}$ coordination, respectively.

Compared with our computations shorter Fe–OH inter-atomic distances are seen of 1.92–1.99 Å with EXAFS. The Fe–OH distance might be slightly shorter than this observed in the crystallographic structure [5]. The two coordinated benzimidazole groups in HPTB give Fe–N bonds of 2.105 Å and a longer Fe–N inter-atomic distance of 2.327 Å for the amine N. The two coordinated pyridine groups in HPTP give Fe–N bonds of 2.185 Å and a longer Fe–N inter-atomic distance of 2.384 Å for the amine N. The

large Debye–Waller factor arises from the wide range of Fe–ligand bond lengths in a sample consisting of several different species.

Table 2
Mössbauer spectral data for enzymes and their mimics^a

Species	δ (mm/s) ^c	Δ (mm/s)	Relative intensity (%)
$[\text{Fe}(\text{Sq}^b)(\text{OH})(4\text{-Me-py})]_2$	0.33	0.55	100
$[(N\text{-base})\text{PcFe}]_2\text{O}$	0.17–0.20	1.6–1.76	100
$[\text{Fe}_2\text{O}(\text{Oac})_2(\text{HBpz}_3)_2]$	0.52	1.60	100
$[\text{Fe}_2\text{O}(\text{Oac})_2(\text{bpy})_2(\text{Cl})_2]$	0.37	1.80	100
Methemerythrin	0.46	1.57	100
Oxyhemerythrin	0.52	1.92	50
Oxyhemerythrin	0.48	1.00	50
$[\text{Fe}_2(N\text{-Et-HPTB})(\text{OBz})]$	1.07	3.13	100
$[\text{Fe}_2\text{O}_2(N\text{-Et-HPTB})(\text{OBz})]$	0.52	0.72	100
$[\text{Fe}_2(\text{H}_2\text{Hbab})_2(N\text{-MeIm})_2]$	0.52	3.26	100

^a From [4–12,18–23].

^b Squarate, $\text{C}_4\text{O}_4^{2-}$.

^c Values are expressed relative to metallic Fe at 300 K.

Table 3
Universal force field (UFF) bond stretch types

	R_{ij}	K_{ij}	R_{ijn}	K_{ijn}	$R_{ijn} - R_{ij}$
Fe ₃ + 2N ₂	2.080000	549.4361	2.0367	585.2129	-0.0433
Fe ₃ + 2O-R	2.050000	500.5698	1.9666	566.9955	-0.0834
O-R-H	1.034000	984.3983	1.0121	1049.6934	-0.0219
O-R-C ₃	1.437000	984.1528	1.4156	1029.5547	-0.0214

Table 4
Universal force field (UFF) angle bending types

	K_{ijk}	θ_0 (bond angle)	p (Period cosine)
Fe ₃ + 2N ₂ -H	85.1612	111.3000	0.0741
Fe ₃ + 2N ₂ -C ₂	180.2790	111.3000	0.0584
Fe ₃ + 2O-R-H	64.9427	128.0000	0.0565
Fe ₃ + 2O-R-C ₃	131.2754	126.4000	0.0425
Fe ₃ + 2OR-Fe ₃ + 2	179.5816	105.4000	0.0458
N ₂ -Fe ₃ + 2N ₂	176.1039	109.4710	0.0410
O-RFe ₃ + 2N ₂	159.8253	109.4710	0.0411
O-R-Fe ₃ + 2-O-R	436.2154	74.5000	0.1242

3.2. Computational analysis

3.2.1. Modeling the structures

The [Fe₂(HPTP)(μ -OH)]⁴⁺ (1), and [Fe₂(HPTB)(μ -OH)]⁴⁺ (2) complexes are used in catalysis. These are models that have a structure that combines all the features of the ligand and the iron active site. The [Fe₂(HPTM)(μ -OH)]⁴⁺ complex was used in the calculations and an iminomethyl group is positioned where a pyridine or a benzimidazole occur in the actual ligands as seen in Fig. 1. Both ferric [Fe₂(HPTM)(μ -OH)]⁴⁺ and ferrous [Fe₂(HPTM)(μ -OH)]²⁺ cores are then optimized with quantum mechanics (QM). Compared with our EXAFS data the Fe-Fe distance of 3.135 Å obtained on the [Fe₂(HPTM)(μ -OH)]⁴⁺ model complexes is intermediate to this of the experimentally studied complexes. The QM optimized structure of [Fe₂(HPTM)(μ -OH)]⁴⁺ is reacted with oxygen in an acidic medium to give intermediates P and Q as shown in Fig. 3. Their interactions with CH₄ will be discussed elsewhere [22].

The charge of the [Fe₂(HPTM)(μ -OH)]^{x+} cluster is +4 or +2, depending on the simulation of a Fe(III) or an Fe(II) active site and the energy levels of different multiplicity are studied. The bond lengths and angles obtained by UFF are the approximate starting point.

The relative energies of some important catalytic reactants were analyzed, as are the effects of their solvation again obtained by QM calculations. The UFF bond stretch types, angle bending types and Lennard-Jones 12-6 parameters for the model complexes have been determined as seen in Tables 3–6. Due to the change of a ferrous to a ferric type, the decrease in the bond length and the increase in the force constant for the Fe-X bond are seen and some changes in the angle bending parameters are observed. Only a slight increase is seen for the angles of the N₂ from 111.2 to 111.3°, these for the O-R increase from the standard 110–128.0 and 126.4° in the diferric core. Also, a decrease of the O-R Fe O-R angle can be seen from 90

Table 5
Universal force field (UFF) Lennard-Jones 12-6 parameters

	X_{ij} ^a	D_{ij} ^b	Scale ζ ^c
H	2.88600	0.04400	12.00000
C ₃ and C ₂	3.85100	0.10500	12.73000
N ₃ and N ₂	3.66000	0.06900	13.40700
O-R	3.50000	0.06000	14.08500
Fe ₃ + 2	2.91200	0.01300	12.00000

^a Van der Waals bond length in Å.

^b Well depth in kcal/mol.

^c The scale factor ζ shows that a Lennard-Jones exponential 6 form is chosen.

Table 6
Geometries of the complexes from experiment and force fields^a

	Experiment	MSX	UFF
Fe–O/Fe–N	1.946	1.900	1.852/2.080
Fe–O	2.116	2.099	2.135/2.050
Fe–O–Fe	119.7	123.4	91.6/109.471
O–Fe–O	102.5	102.8	80.5/74.5

^a Experimental data from XRD, EXAFS and IR correlations [9] and force fields: material simulation X (MSX) and universal force field (UFF) after [13,14].

to 74.5°. The N₂Fe₃ + 3N₂ angles remain constant at 109.47°.

The complex has C_{2h} symmetry and both ferrous iron ions can occur either in a high-spin quintet state, and intermediate-spin triplet state or a low-spin singlet state, when these states couple, we obtain a non-uplet state if the two iron ions are high-spin,

$$N \quad (dxz)^2(dxz)(dyz)(dz^2)(dx^2 - y^2)$$

the quintet state Q, if the two iron ions are intermediate-spin,

$$Q \quad (dxz)^2(dxz)(dyz)(dz^2)$$

or singlet S, when the two iron ions are in low-spin form.

$$S \quad (dxz)^2(dxz)(dyz)(dz^2)$$

When both ferric iron ions can occur either in a high-spin sextet state, and intermediate-spin quartet state or a low-spin doublet state, when these states couple we obtain the undecuplet state if the two iron ions are high-spin,

$$U \quad (dxz)(dxz)(dyz)(dz^2)(dx^2 - y^2)$$

the septet state, SP if the two iron ions are intermediate-spin,

$$SP \quad (dxz)^2(dxz)(dyz)(dz^2)$$

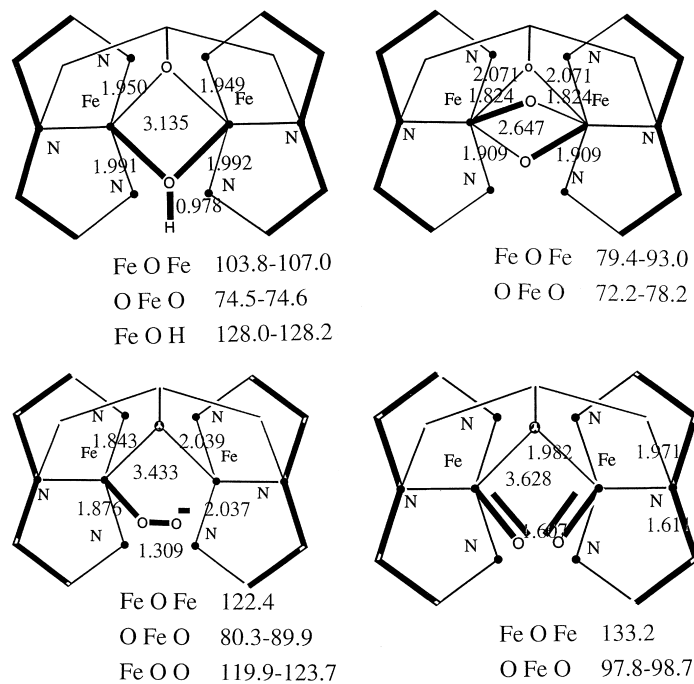


Fig. 2. QM optimized structures of [Fe₂^{II}(HPTM)(μ-OH)]²⁺ of [Fe₂^{III}(HPTM)(μ-O₂)₂]³⁺ of [(Fe^{IV}=O)₂(HPTM)]³⁺ and of [Fe₂^{III}(μ-O)₂(HPTM)(μ-O)₂]³⁺. The interatomic FeO, Fe–Fe, O–O and O–H distances (Å) and FeOFe, FeOO, FeOH and OFeO angles (°) are given in and under the figure respectively.

or triplet T, when the two iron ions are in low-spin form.

$$T \quad (dxz)^2(dxz)(dyz)$$

In the ferric case (Fe^{III}), the septet (SP) and the undecuplet (U) are its ground state and low lying excited states. The equatorial (*trans*) and axial (*cis*) effect of the N atoms with respect to the bridging μ -oxo groups dictate their bond lengths that are 2.03–2.04, 2.31 and 1.95–1.99 Å, respectively. The bond distances of 1.95 and 1.99 Å obtained from QM seen in the direction of the equatorial unprotonated and protonated O groups compared to the calculations, are accompanied by Fe–O–Fe angles close to the 90–93° and to a O–Fe–O bite angle of 74.5°. The Fe coordinated to the axial N group has long bond distances of 2.31 Å seen in the QM calculations. The bond length of Fe to the equatorial N groups show short bond distances of 2.03–2.04 Å seen in the QM calculations, the N–Fe–N bite angle varies around values of 110.0° in QM. In QM, the order of the angles is such that Fe–O–R >

Fe–N–R > Fe–O–Fe–N–Fe–N > O–Fe–O, in particular the first two values are much higher in QM compared to UFF and the last two values are much lower in QM compared to UFF. In UFF the N–Fe–N angles are larger than the Fe–O–Fe angles. Such QM data are used to change UFF parameters as seen in Tables 3–6 to better position the ligands (HPTB, HPTP) and allow to study larger systems with QM-parametrized modified UFF parameters.

3.2.2. Modeling the oxygen activation

Geometrical and electronic properties affect the relative catalytic properties, such as the hydrogen bond abstraction energies of the binuclear cores of these iron complexes. In the QM optimized structure, the iron core has two μ -oxo and six terminating nitrogen atoms, the B3LYP calculations will now be performed on all the reaction intermediates. In these structures differences between the equatorial and axial nitrogen atoms are seen. In aqueous reactions, in acidic media, the bridging by the deprotonated ligand alcohol group remains strong, whereas the bridging (μ -OH)

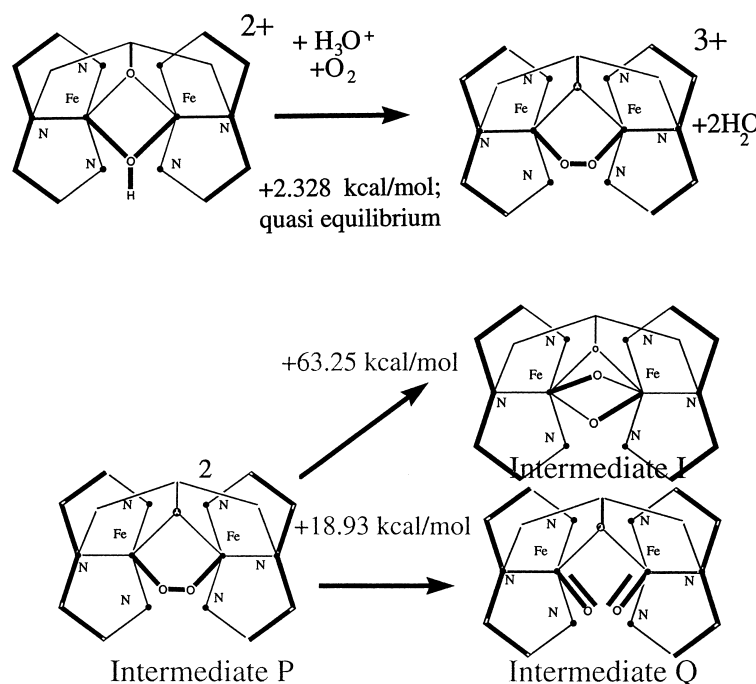


Fig. 3. Reaction scheme for oxygen activation: formation of the peroxo intermediate P and the transformation into intermediate Q which is favored over this to the inactive intermediate I.

can be protonated and removed as water and lead to the binding of molecular oxygen and the consequent transformation of this intermediate into an oxidized bis-ferryl form [26]. During this transformation, the oxygen molecule is transformed in a peroxo (O_2^{2-}) group (intermediate P) with the formal change of the charges of iron from +2 to +3.

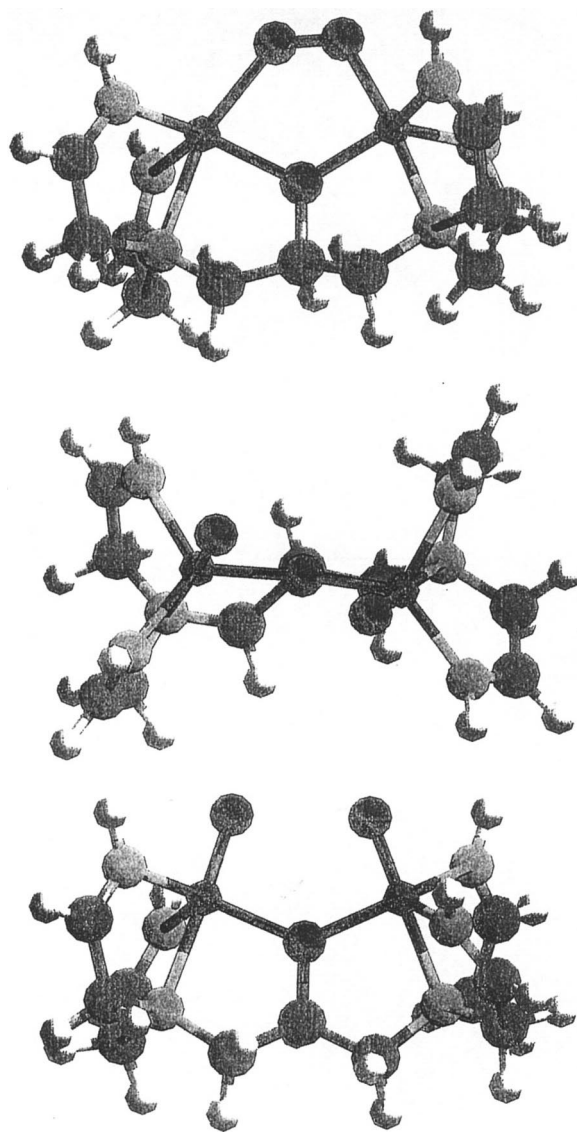


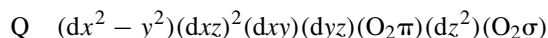
Fig. 4. QM calculated structure of $[Fe_2(HPTM)(\mu-O_2)]^{3+}$ and $[Fe_2(HPTM)(O)_2]^{3+}$ (top and side) model compounds.

This leads to a diamagnetic singlet state



here the dyz orbital is coupled to the two orthogonal three electron pi-system of the O_2 ligands.

The alternative is a paramagnetic quintet state



The two double ferryl type bonds can become stronger by transfer of the sigma bonding electrons between the two oxygen atoms to their anti-bonding orbitals and the pairing of these with an extra electron from the iron ion. In a consequent step the peroxo (O_2^{2-}) group is transformed into two ferryl (O^{2-}) bound groups (intermediate Q), with the formal change of the charges of iron from +3 to +4. In an alternative step, the peroxo (O_2^{2-}) group of the complex can also transform to yield two bridging ($\mu-O$) oxo groups, additional to the ligand bound O, which remains coordinated.

For the diferric complex and the diferrous complex, the high spin state seems to be the ground state. From these calculations it is clear that superexchange coupling for these complexes is fairly small, this agrees with the experimental observation of a J value of 12 cm^{-1} for the diferrous OH bridged model compound [18–20].

The geometrical implications on these reactions are probed with QM B3LYP analysis and the results are shown in Figs. 2–4 and Table 6. The oxygen bond length of 1.21 increases to 1.31 Å on the model compound and is smaller than the 1.49 Å distance in hydrogen peroxide, consequently this bond is broken in the model compound. The $Fe \cdots Fe$ distances in the model compound $[Fe_2(HPTM)(\mu-OH)]^{4+}$ of 3.14 Å increases to 3.43 Å in intermediate P and 3.63 Å in intermediate Q. Upon transformation into the bis ($\mu-O^{2-}$) oxo bridged dimer, this distance decreases to 2.65 Å. The energy of the different intermediates seem fairly comparable with the peroxo form or intermediate P, being slightly more stable than the ferryl form or intermediate Q by about 18.9 kcal/mol. The formation of the bis ($\mu-O^{2-}$) oxo seems unfavorable since it is 44.4 kcal/mol higher in energy. The charges have been analyzed by Q_{eq} and electrostatic potential QC_{ESP} charge fitting as seen in Table 7. Solvation proves higher in complexes with

Table 7
Charges of the $[\text{Fe}_2(\text{O}=\text{O})_2(\text{O})\text{L}]^{3+}$ complex from QC and Qeq*^a

	QC _{ESP}	Qeq*N
Fe	+1.158, +1.188	+1.104, +1.116
–O–	–0.765	–0.443
O=	–0.290, –0.301	–0.425
H	+0.420 +0.050	+0.191, +0.050
N	–0.704, –0.621	–0.285, –0.275
N	+0.466, +0.363	–0.419, –0.409
C	–0.447, –0.498	–0.137, –0.128
C(–O–)	+0.364, +0.321	+0.110

^a Electronegativities are $X_{\text{Fe}} = 3.5$, $X_{\text{O}} = 8.741$, $X_{\text{C}} = 5.343$, $X_{\text{N}} = 6.899$, $X_{\text{H}} = 4.528$. Hardness and radius for Fe are modified to $1/2J_{\text{Fe}} = 3.124$ and $R_{\text{Fe}} = 1.293$, respectively.

increased charge transfer, i.e. Fe(IV)-complexes are better stabilized by solvation than Fe(III)-complexes. The solvation calculations given in Table 8 are important to obtain good quantitative data of the overall reactivity of the system. The solvation calculations use a Poisson–Boltzmann type solvation assuming a dielectric constant of water ($\epsilon=80.37$) and a known probe radius (1.40 Å). As the organic part of the complex renders the core hydrophobic and most of the reactions are performed in water–acetonitrile mixtures, the choice to study the B3LYP QM of the entire organic complexes is new [3]. The solvation energy is about 150, 300 and 500 kcal/mol for the +2, +3 and +4 complexes, respectively, and fits the reaction data well.

3.2.3. Description of the orbitals involved in the reactive site

The frontier orbitals for the ground state iron core with a μ -carboxy back-bone and a μ -oxo group or μ -hydroxo group have significant d-character. The unpaired valence electrons on the individual iron cores can also be localized primarily in the d-orbitals. The undecuplet for the oxidized and the non-aplet for the

reduced resting state model has the lowest energy. For the intermediate Q, the orbitals that participate at the active site were studied. In Fig. 5, the most relevant binding orbitals are seen, the Fe–O covalent σ -bond and the C–O σ -bond as well as the σ - and π -bonds of the ferryl Fe=O in the plane of the Fe–O–Fe bridge can be seen. The active bis-ferryl μ -oxo-bridged site shows eight unpaired electrons. The localization of these free d-electrons occurs partially on the iron (Fe^{IV}) like with a spin density of 2.6 to 2.8) and partially on the oxygen (spin density around 0.80 and 0.85). Siegbahn [3] found that the spin on iron varies from 4.00 on Fe^{III} , 3.75 on Fe^{II} and 3.2 on Fe^{IV} . As implied by the spin density analysis, the nature of the ferryl is closer to a two atom three-electron bond as to a double bond involving four electrons. During the transformation, the oxygen molecule is transformed in a peroxo (O_2^{2-}) group (intermediate P) and a bis-ferryl μ -oxo-bridged site with the change of the formal charges of iron from +2 to +3 and +4. Siegbahn [3] found that due to the large Jahn–Teller distortions in the d^4 bis- μ -oxo species the Fe–O–Fe bridges are highly asymmetric, allowing the system to open up easily to a key $\text{Fe}^{\text{III}}-\text{O}-\text{Fe}^{\text{V}}=\text{O}$ intermediate that can react with methane via a low-energy transition state. This intermediate $\text{Fe}^{\text{III}}-\text{O}-\text{Fe}^{\text{IV}}-\text{O}^0$ with radical character at the terminal oxo-group is in accordance with our spin localization. After the H abstraction from methane, the methyl radical recombines rapidly with the Fe center via a weak Fe–CH₃ bond in his model and with the loss of methanol $\text{Fe}^{\text{III}}-\text{O}-\text{Fe}^{\text{III}}$ is formed which can be reduced to the Fe(II, II) form.

3.3. Diffuse reflectance spectroscopic (DRS) analysis

The oxygen adducts of the binuclear Fe(II)-complexes are formally analogous to the peroxide adducts of the Fe(III)-complexes e.g. oxy-hemerythrin

Table 8
Relative solvation energies obtained by QM calculations for active intermediates of the complexes in which (O)L = HPTM and M = model C=N

Species, charge	Absolute energy (hartrees)	M	Spin	Energy difference (kcal/mol)
$[\text{Fe}_2(\text{OH})(\text{O})\text{L}]^{2+}$	–1158.405161	9	4	155
$[\text{Fe}_2(\text{OH})_2(\text{O})\text{L}]^{3+}$	–1234.245871	7	3	335
$[\text{Fe}_2(\text{O}=\text{O})_2(\text{O})\text{L}]^{3+}$	–1232.996704	9	4	340
$[\text{Fe}_2(\text{OH})(\text{O})\text{L}]^{4+}$	–1158.653119	9	4	592

Electronic Nature of Int. Q

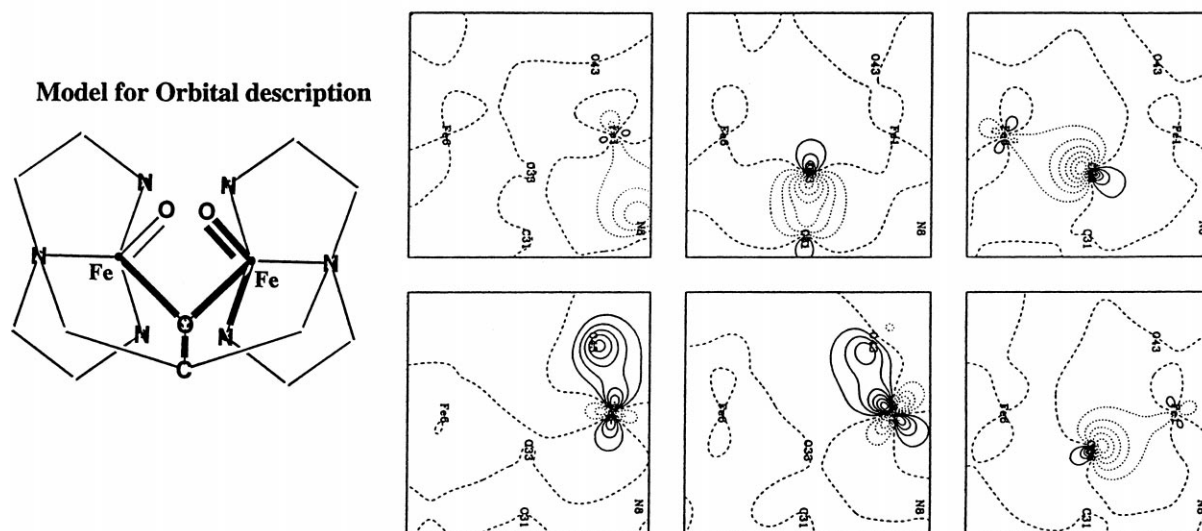


Fig. 5. Orbital maps of the intermediate Q active site for which the different bonds in the Fe–O–Fe=O plane of the $[\text{Fe}_2(\text{HPTM})(\text{O})_2]^{3+}$ structure can be visualised.

[4] as two electron transfers occur in these systems. Partial charge redistribution can occur after peroxide \rightarrow Fe interaction. Concomitant changes in the ligand iron distances lead to changes in the coordination of benzimidazole or pyridine with Fe. With DRS in the UV–VIS region, d–d, π – π^* transitions, and charge transfer between metal and ligand such as metal–ligand charge transfer MLCT and ligand–metal charge transfer (LMCT) can be probed. The spectrum of $[\text{Fe}_2(\text{HPTB})(\text{OH})(\text{NO}_3)_2](\text{NO}_3)_2$ shows λ_{max} at 340 nm, due to the benzimidazole–iron charge transfer. The spectrum of $[\text{Fe}_2(\text{HPTP})(\text{OH})(\text{NO}_3)_2](\text{ClO}_4)_2$ shows λ_{max} at 290 nm, of a pyridyl–iron charge transfer. DRS-spectra of $[\text{Fe}_2(\text{HPTB})(\text{OH})(\text{NO}_3)_2](\text{NO}_3)_2$ show their charge transfers at higher wavelengths compared to the $[\text{Fe}_2(\text{HPTP})(\text{OH})(\text{NO}_3)_2](\text{NO}_3)_2$ complexes (Fig. 6). Maxima occur at 340 and 500 nm for $[\text{Fe}_2(\text{HPTB})(\text{OH})(\text{NO}_3)_2](\text{NO}_3)_2$ and at 355 and 490 nm with a shoulder at 600 nm for the $[\text{Fe}_2(\text{HPTP})(\text{OH})(\text{NO}_3)_2](\text{ClO}_4)_2$ complexes. From 300–400 nm oxo \rightarrow Fe CT transitions are seen and for the bent Fe–O–Fe geometries three π -derived transitions of oxo p_x , p_y , p_z –Fe d_{xz} , d_{yz} and $d_{x^2-y^2}$ are expected. In the 440–510 nm, region pairs of ab-

sorption bands due to the bent Fe–O–Fe with 10-fold lower intensity are seen if carboxylato, carbonato or phosphate-bridges are present. Peroxo \rightarrow Fe CT absorption arise between 400 and 500 nm upon addition of peroxides to the catalysts in methanol [26]. Both $[\text{Fe}_2(\text{HPTP})(\mu\text{-OH})(\text{NO}_3)_2](\text{ClO}_4)_2$ (1) and $[\text{Fe}_2(\text{HPTB})(\mu\text{-OH})(\text{NO}_3)_2](\text{ClO}_4)_2$ (2) form blue–violet adducts with H_2O_2 . Easy formation of a 1:1 adduct of $[\text{Fe}_2(\text{HPTB})(\text{OH})(\text{NO}_3)_2](\text{NO}_3)_2$ and

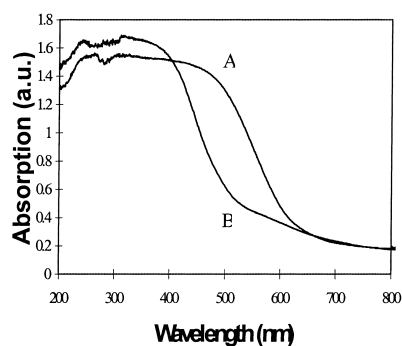


Fig. 6. DRS-spectra of $[\text{Fe}_2(\text{HPTB})(\text{OH})(\text{NO}_3)_2](\text{NO}_3)_2$ (A) and $[\text{Fe}_2(\text{HPTP})(\text{OH})(\text{NO}_3)_2](\text{ClO}_4)_2$ (B).

H₂O₂ are analogous to interaction of the reduced complex with O₂ in CH₂Cl₂ at –60°C to allow irreversible O₂ binding.

4. Conclusions

The reaction of the MMO mimic binuclear heptapodate coordinated iron(III)-complexes of *N,N,N',N'*-tetrakis(iminomethyl)-2-hydroxy-1,3-diamino-propane (HPTM) model with oxygen is studied. When one bridging ligand is removed from each ferrous iron the μ - η^1 : η^1 -O₂ binding proves the most favorable binding mode of dioxygen on complexes. This forms the so-called intermediate P (peroxo form), that can convert in the intermediate Q (bis-ferryl form) with little structural reorganization and this requires a moderate energy input of about 18.9 kcal/mol in order to facilitate the removal of two water molecules, the peroxo-bond cleavage and the formal oxidation of Fe^{III}–Fe^{IV}. The [Fe₂(HPTP)(μ -OH)]⁴⁺ and [Fe₂(HPTB)(μ -OH)]⁴⁺ model complexes are characterized with EXAFS to study the Fe–Fe and Fe–ligand bonding, the Fe–Fe distances are 3.020 and 3.223 Å, respectively, in accordance with the crystallographic data and the quantum mechanic value of 3.135 Å obtained on the [Fe₂(HPTM)(μ -OH)]⁴⁺ model complexes. The σ - and π -bonds of the ferryl Fe=O in the plane of the Fe–O–Fe bridge, were analyzed and show that the nature of this ferryl species is this of a two atom three electron bond.

Acknowledgements

PPKG would like to thank the Belgian Fund for Scientific Research (FWO-FNRS), the UCL and, Atsushi Fukuoka and Masaru Ichikawa from the Catalysis Research Center, at Hokkaido University, Sapporo 060, Hokkaido, Japan for a collaboration on EXAFS.

References

- [1] K. Yoshizawa, K. Ohta, T. Yamabe, R. Hoffmann, J. Am. Chem. Soc. 119 (1997) 12311.
- [2] R.H. Crabtree, Chem. Rev. 95 (1995) 987.
- [3] P.E. Siegbahn, R.H. Crabtree, J. Am. Chem. Soc. 119 (1997) 3103.
- [4] Y. Dong, S. Yan, V.G. Young Jr., L. Que Jr., Angew. Chem. 108 (1996) 674.
- [5] A.C. Rosenzweig, C.A. Frederick, S.J. Lippard, P. Nordlund, Nature 366 (1993) 537.
- [6] K.E. Liu, D. Wang, B.H. Huynh, D.E. Edmonson, A. Salifoglou, S.J. Lippard, J. Am. Chem. Soc. 116 (1994) 7465.
- [7] K.E. Liu, A.M. Valentine, D. Qiu, D.E. Edmonson, E.H. Appelman, T. Spiro, S.J. Lippard, J. Am. Chem. Soc. 117 (1995) 4997.
- [8] S.J. Lippard, Angew. Chem. Int. Ed. Eng. 27 (1988) 344.
- [9] D.M. Kurtz, Chem. Rev. 90 (1990) 585.
- [10] L. Que, Y. Dong, Acc. Chem. Res. 29 (1996) 190.
- [11] T.M. Loehr (Ed.), Iron Carriers and Proteins, VCH, Weinheim, 1989, p. 373.
- [12] L. Shu, J.C. Nesheim, K. Kauffmann, E. Munck, J.D. Lipscomb, L. Que Jr., Science 275 (1997) 515.
- [13] A.K. Rappé, C.J. Casewit, K.S. Colwell, W.A. Goddard, W.M. Skiff, J. Am. Chem. Soc. 114 (1992) 10024.
- [14] A.K. Rappé, W.A. Goddard, J. Chem. Phys. 95 (1991) 3358.
- [15] References in the Jaguar User Guide.
- [16] P.P. Knops-Gerrits, P.A. Jacobs, W.A. Goddard III, Stud. Surf. Sci. Catal., 130 D, Proceedings of the 12th Int. Congress on Catalysis, A. Cama et al. (Eds.), (2000) 1187.
- [17] S. Shaik, M. Filatov, D. Schröder, H. Schwarz, Chem. Eur. J. 4 (1998) 193–199.
- [18] S. Menage, B.A. Brennan, C. Juarez-Garcia, E. Munck, L. Que Jr., J. Am. Chem. Soc. 112 (1990) 6423.
- [19] R.G. Wilkins, Chem. Soc. Rev. (1992) 171–178.
- [20] P.C. Wilkins, R.G. Wilkins, Coord. Chem. Rev. 79 (1987) 195–214.
- [21] R.E. Norman, R.C. Holz, S. Menage, L. Que Jr., Y. Zhang, J.H. O'Connor, Inorg. Chem. 29 (1990) 4629.
- [22] G.T. Babcock, M. Wikstrom, Nature 356 (1992) 301.
- [23] N. Kitajima, H. Fukui, Y. Moro-oka, Y. Mizutani, T. Kitagawa, J. Am. Chem. Soc. 112 (1990) 6402.
- [24] P.P. Knops-Gerrits, A. Weiss, S. Dick, P.A. Jacobs, Stud. Surf. Sci. Catal. 110 (1997) 1061.
- [25] P.P. Knops-Gerrits, A.M. Van Bavel, G. Langouche, P.A. Jacobs, in: Derouane, et al. (Eds.), Proceedings of the NATO ASI, 1998, 3.44, p. 215.
- [26] P.P. Knops-Gerrits, A. Verberckmoes, R.A. Schoonheydt, M. Ichikawa, P.A. Jacobs, Microporous Mesoporous Mater. 21 (4-6) (1998) 475.
- [27] I. Vankelcom, K. Vercruysse, P.E. Neys, D. Tas, K. Janssen, P.P. Knops-Gerrits, P.A. Jacobs, Topics in Catalysis 5 (1998) 125–132.
- [28] P.P. Knops-Gerrits, Xiao-yuan Li, W.A. Goddard III, Raman Spectroscopy, S.-L. Zhang, B.-F. Zhu (Eds.), Wiley (2000) 782.